ISSN 1063-7761, Journal of Experimental and Theoretical Physics, 2012, Vol. 114, No. 1, pp. 118–131. © Pleiades Publishing, Inc., 2012.
Original Russian Text © S.V. Nikolaev, S.G. Ovchinnikov, 2012, published in Zhurnal Eksperimental'noi i Teoreticheskoi Fiziki, 2012, Vol. 141, No. 1, pp. 135–150.

ELECTRONIC PROPERTIES OF SOLID

Effect of Hole Doping on the Electronic Structure and the Fermi Surface in the Hubbard Model within Norm-Conserving Cluster Pertubation Theory

S. V. Nikolaev[a,b] and S. G. Ovchinnikov[a,c]

[a] *Kirensky Institute of Physics, Siberian Branch, Russian Academy of Sciences, Krasnoyarsk, 660036 Russia*
[b] *Dostoevsky State University, Omsk, 644077 Russia*
[c] *Siberian Federal University, Krasnoyarsk, 660041 Russia*
e-mail: 25sergeyn@mail.ru; sgo@iph.krasn.ru

Received May 3, 2011

Abstract—The concentration dependences of the band structure, spectral weight, density of states, and Fermi surface in the paramagnetic state are studied in the Hubbard model within cluster pertubation theory with 2×2 clusters. Representation of the Hubbard X operators makes it possible to control conservation of the spectral weight in constructing cluster perturbation theory. The calculated value of the ground-state energy is in good agreement with the results obtained using nonperturbative methods such as the quantum Monte Carlo method, exact diagonalization of a 4×4 cluster, and the variational Monte Carlo method. It is shown that in the case of hole doping, the states in the band gap (in-gap states) lie near the top of the lower Hubbard band for large values of U and near the bottom of the upper band for small U. The concentration dependence of the Fermi surface strongly depends on hopping to second (t') and third (t'') neighbors. For parameter values typical of HTSC cuprates, the existence of three concentration regions with different Fermi surfaces is demonstrated. It is shown that broadening of the spectral electron density with an energy resolution typical of contemporary ARPES leads to a pattern of arcs with a length depending on the concentration. Only an order-of-magnitude decrease in the linewidth makes it possible to obtain the true Fermi surface from the spectral density. The kinks associated with strong electron correlations are detected in the dispersion relation below the Fermi level.

DOI: 10.1134/S1063776111150143

1. INTRODUCTION

It is well known that high-temperature superconducting cuprates belong to the class of materials with strong electron correlations (SECs). Recent investigations of high-temperature superconductors (HTSCs) by scanning tunnel spectroscopy (STS) and angle-resolved photoemission spectroscopy (ARPES) have revealed a number of characteristic features of the normal phase of such materials [1, 2]. First, this concerns the existence of a pseudogap in a wide doping range [3–6]. Several theories for the origin of the pseudogap have been developed, but it still remains unclear. The second distinguishing feature of such materials is a peculiar dependence of the Fermi surface on the doping level. ARPES experiments have revealed the existence of an arc structure associated with a nonuniform distribution of the spectral weight of Fermi quasiparticles over the Fermi surface [7–9]. The results of theoretical calculations indicate the presence of a pocket in the vicinity of point $(\pi/2, \pi/2)$ in the first quadrant of the first Brillouin zone under weak doping [10–15]. The specific behavior of the Fermi surface in the region of the pseudogap state is manifested in different values of the electron spectral weight in different regions of the surface [10]. Another experimentally observed feature is the sharp variation in the slope of the dispersion curve (kink) below the Fermi level [7, 16]. The emergence of the kink is attributed to the electron–phonon interaction and to the spin-fluctuation mechanism, as well as with the purely electron–electron interaction due to correlation effects [17, 18].

In attempts at interpreting the origin of high-temperature superconductivity in doped Mott–Hubbard insulators, the main attention was concentrated on analyzing the changes in the topology of the Fermi surface with the doping level. In [10], the evolution of the Fermi surface is described using the spin–polaron approach. The doping level is taken into account in the frustration parameter in the spin Hamiltonian. The changes in the Fermi surface in HTSC cuprates were investigated in [11] using the effective p–d Hubbard model. The arc structure of the Fermi state in the weak doping range was revealed. The origin of kinks on the dispersion curves was also considered. Quantum phase transitions were studied in [12, 15] using the generalized tight binding method with ab initio calculations of the (GTB + LDA) model parameters. These calculations were performed for the LSCO system and

showed good qualitative agreement with experimental data. In particular, the existence of a pocket near point $(\pi/2, \pi/2)$ in the range of weak doping was demonstrated; upon a transition through critical point p_{c1}, this pocket is transformed into two pockets in the vicinity of point (π, π) in the weak-doping region; after the transition through the second critical point p_{c2}, only one large surface around point (π, π) is left. Analogous results were also obtained within the cluster generalization of the dynamic mean field theory (CDMFT) [14, 19].

In this study, we use the cluster approach, which has been widely employed in recent years [20]. The advantage of this approach is that SECs and the short-range order, which plays a significant role in the description of low-dimensional magnetic systems, are taken into account directly. The foundation of this method was laid long ago and was successfully employed in analyzing HTSC cuprates in [21–23]. The cluster perturbation theory contains two main stages in constructing the solution; the first stage involves the choice of the cluster taking into account the symmetry of the initial lattice and the construction of intrinsic multielectron states for the given cluster using the exact diagonalization method; at the second stage, the intercluster interaction is taken into account in perturbation theory. In this study, we are using the Hubbard model [24] written in the representation of Hubbard operators [25] (X representation) as the basic mode. The cluster is chosen in the form of a 2×2 square with four sites. Such a configuration fully reflects the symmetry of the initial lattice. The X representation makes it possible to easily pass from the Hamiltonian of the initial lattice to the cluster Hamiltonian and to obtain the solution for the Green's function in the Hubbard-I approximation. It was shown in [26] that the X representation makes it possible to introduce the concept of the f-factor, which determines the measure of the spectral weight for a Fermi quasiparticle. The control over this quantity at the first stages of calculation makes it possible to reduce the computer time without introducing noticeable distortions in the final result of computation.

The structure of the article is as follows. In Section 2, the cluster perturbation theory in the X representation is briefly considered. We describe the procedure of determining the Green's function for an infinite lattice in the antiferromagnetic and paramagnetic states. The scheme of formation of Hubbard quasiparticles for a nonzero doping level is presented. In Section 3, the proposed method is tested by calculating the dependence of the ground-state energy on Coulomb interaction parameter U and on the concentration; the results are compared with those obtained by other authors. In Section 4, the formation of in-gap states and the redistribution of the spectral weight among these states and Hubbard subbands are described. In Section 5, the evolution of the Fermi surface upon a variation in the hole concentration is considered. The effect of hopping between the second and third nearest neighbors on the spectral weight redistribution in the dispersion relation and on the Fermi surface is analyzed in Section 6. Section 7 contains a discussion and qualitative comparison of our results with those obtained in other experimental and theoretical works.

2. METHOD

In this study, we confine our analysis to a 2D square lattice. The Hubbard model is undoubtedly a good approximation for describing systems with strong electron correlations [24]. In spite of its apparent simplicity, this model, which was proposed more than 40 years ago, is extremely rich from the physical point of view and remains a basic model for analyzing a large class of materials with SECs. The Hamiltonian of the 2D one-band Hubbard model has the form

$$H = \sum_{i\sigma}\left\{(\varepsilon-\mu)n_{i\sigma} + \frac{U}{2}n_{i\sigma}n_{i\bar{\sigma}}\right\} - \sum_{i\neq j,\,\sigma} t_{ij}a^{\dagger}_{i\sigma}a_{j\sigma}, \quad (1)$$

where $a^{\dagger}_{i\sigma}$ and $a_{i\sigma}$ are the creation and annihilation operators for an electron with spin σ at the ith site; $n_{i\sigma} = a^{\dagger}_{i\sigma}a_{i\sigma}$ is the operator of the number of electrons with spin σ ($\bar{\sigma} = -\sigma$); ε is the electron energy at the site; μ is the chemical potential; t_{ij} is the hopping integral from site j to site i; and U is the parameter of the Coulomb interaction at the site.

For the unit cell, we choose a square 2×2 cluster and regroup the terms in Hamiltonian (1) so that the intracluster interactions are separated from the intercluster interactions:

$$H = \sum_{f} H_0^c(f) + \sum_{f\neq g} H_1^c(f,g), \quad (2)$$

where f and g are the cluster indices. The subsequent procedure includes calculation of the complete set of eigenstates and eigenvectors of Hamiltonian $H_0^c(f)$ by the exact diagonalization method, as well as the construction of the corresponding cluster X operators and the transition to Hamiltonian H in the X representation. As a result, for the operator of electron annihilation at site i belonging to cluster f, we obtain the following representation:

$$a_{i\sigma} = \sum_{\alpha}\gamma_{i\sigma}(\alpha)X_f^{\alpha}, \quad \gamma_{i\sigma}(\alpha) = \langle n|a_{i\sigma}|m\rangle, \quad (3)$$

indicating that the electron is described by a superposition X_f^{α} of various quasiparticles (Hubbard fermions), each of which corresponds to the excitation from the multielectron initial state $|m\rangle$ to the multielectron final state $|n\rangle$. This procedure was described in greater detail in [26]. Here, we have used the following nota-

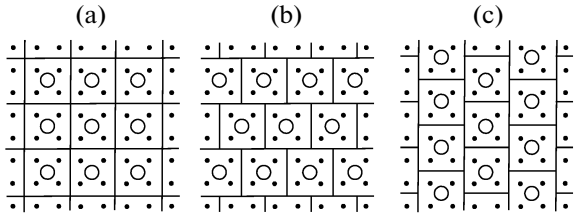

Fig. 1. Possible version of coverage of the initial square lattice by 2 × 2 clusters. Points and circles denote the sites of the initial lattice and of the cluster superlattice, respectively. The following notation for covers is used in the text: $K1$ (a), $K2$ (b), and $K3$ (c).

tion for the X operators: $X_f^\alpha \equiv X_f^{nm} = |n\rangle\langle m|$, where $\alpha = \alpha(n, m)$; n and m are the final and initial states of the cluster, respectively; and f is the cluster index. A more detailed description of the properties of X operators can be found in [25, 27–29]. After transformations, Hamiltonian (2) assumes the form

$$H = \sum_{fn} \varepsilon_n X_f^{nn} + \sum_{f \neq g} \sum_{\alpha\beta} t_{fg}^{\alpha\beta} X_f^{+\alpha} X_g^\beta, \tag{4}$$

where ε_n is the energy of the cluster in state n and $t_{fg}^{\alpha\beta}$ are hopping integrals between clusters.

Taking into account the homogeneity conditions, we can write Hamiltonian (4) in terms of the reciprocal space:

$$H = \sum_{\tilde{k}} \sum_{n} \varepsilon_n X_{\tilde{k}}^{nm} + \sum_{\tilde{k}} \sum_{\alpha\beta} T_{\alpha\beta}(\tilde{\mathbf{k}}) X_{\tilde{k}}^{\dagger\alpha} X_{\tilde{k}}^\beta, \tag{5}$$

where $\tilde{\mathbf{k}}$ is the wavevector assuming the values in the reduced Brillouin zone. This computation step will be considered again at a later stage.

Using the Hubbard-I approximation for intercluster hopping $T_{\alpha\beta}(\tilde{\mathbf{k}})$, we can obtain the solution for the Green's function $D_{\alpha\beta}(\tilde{\mathbf{k}}, \omega) = \langle\langle X_{\tilde{k}}^\alpha | X_{\tilde{\mathbf{k}}}^{\dagger\beta} \rangle\rangle_\omega$ in the following matrix form:

$$D^{-1}(\tilde{\mathbf{k}}, \omega) = (D^0(\omega))^{-1} - T(\tilde{\mathbf{k}}), \tag{6}$$

where

$$D_{\alpha\beta}^0(\omega) = \frac{F(\alpha)}{\omega - \Omega(\alpha)} \delta_{\alpha,\beta}, \tag{7}$$

$$\Omega(\alpha) = \varepsilon_m(N+1) - \varepsilon_n(N) - \mu, \tag{8}$$

$$F(\alpha) \equiv F(n, m) = \langle X^{nn} \rangle + \langle X^{mm} \rangle. \tag{9}$$

Here, $D^0(\omega)$ is the local (cluster) Green's function; $F(\alpha)$ is the filling factor, μ is the chemical potential, and N is the number of electrons in a cluster.

The relation connecting the electron Green's function $G_\sigma(\mathbf{k}, \omega) = \langle\langle a_{k\sigma} | a_{k\sigma}^\dagger \rangle\rangle_\omega$ defined on the initial lattice with the Green's function in the X representation, which is defined on the superlattice, has the form [26, 30]

$$G_\sigma(\mathbf{k}, \omega) = \frac{1}{N_c} \sum_{\alpha\beta} \sum_{i,j=1}^{N_c} \gamma_{i\sigma}(\alpha) \gamma_{j\sigma}^*(\beta) \times D_{\alpha\beta}(\mathbf{k}, \omega) e^{-i\mathbf{k}(\mathbf{r}_i - \mathbf{r}_j)}, \tag{10}$$

where N_c is the number of sites in a cluster (which is four in our case), $\mathbf{k}$ is the wavevector defined in the initial Brillouin zone, and i and j are the indices of the intracluster sites. Here, we have taken into account the fact that Green's function $D_{\alpha\beta}(\tilde{\mathbf{k}}, \omega)$ is a periodic function in the reciprocal space of the superlattice, and wavevector $\mathbf{k}$ can be written in the form $\mathbf{K} + \tilde{\mathbf{k}}$, where $\mathbf{K}$ is the translation vector of the reciprocal superlattice. This allows us to write the equality $D_{\alpha\beta}(\tilde{\mathbf{k}}, \omega) = D_{\alpha\beta}(\mathbf{k}, \omega)$ [20]. Green's function $G_\sigma(\mathbf{k}, \omega)$ and the corresponding spectral function

$$A_\sigma(\mathbf{k}, \omega) = -\frac{1}{\pi} \lim_{\delta \to +0} (\mathrm{Im} G_\sigma(\mathbf{k}, \omega + i\delta + \mu)) \tag{11}$$

are calculated in the initial Brillouin zone.

The total number of states in a 2 × 2 cluster is $4^4 = 256$. When all possible excitations are taken into account exactly in representation (3) of X operators, the sum rule holds:

$$\langle \{ a_{i\sigma}, a_{i\sigma}^\dagger \}_+ \rangle = \sum_\alpha |\gamma_{i\sigma}(\alpha)|^2 F(\alpha) = 1. \tag{12}$$

In the cluster perturbation theory [20, 30], the Lanczos algorithm is used as a rule for determining the ground state and the closest excited states of Hamiltonian H_0. In this case, most of high-energy states are omitted, which violates the sum rule.

In all computations performed in this study, we trace the value of the f-factor introduced in [26] to control the total spectral weight of Fermi quasiparticles:

$$\int d\omega A_\sigma(\mathbf{k}, \omega) = \sum_\alpha |\gamma_{i\sigma}(\alpha)|^2 F(\alpha) \equiv f. \tag{13}$$

Exact calculations yield $f = 1$. All results presented below were obtained for $f > 0.995$. It turned out that the number of energy levels considered here can be substantially reduced, retaining only about 30 states so that the error in the sum rule does not exceed 1%. Therefore, we refer to our version of the cluster perturbation theory with controllable spectral weight as the norm-conserving cluster perturbation theory (NC-CPT).

Let us consider in greater detail the procedure of formation of a cluster lattice (superlattice). The choice of the cluster is a separate problem occupying an important position in cluster theories [20, 30]; however, we will not consider this problem here and confine our analysis to a 2 × 2 cluster. Such a choice of the cluster gives three versions of coverage of the initial

square lattice (see Fig. 1). The first version ($K1$) (Fig. 1a) is the most obvious due to the coincidence of the point symmetry group with the initial lattice and is most widespread. However, the other two versions ($K2$ and $K3$; Figs. 1b and 1c) can also be used in constructing the superlattice. Version $K2$ can be obtained from $K1$ by a displacement of neighboring (along the y axis) chains of clusters by the elementary translation vector of the initial lattice along the x axis, while version $K3$ can be obtained by a displacement along the y axis. Clearly, the point symmetry group in the latter configurations does not coincide with the initial lattice. In this case, the paramagnetic (spatially uniform) and antiferromagnetic (with a reduced Brillouin zone) states are possible. Cover $K1$ corresponds to the antiferromagnetic state [20]. This clear from the dispersion curve depicted in Fig. 2a, on which splitting of the upper and lower Hubbard bands takes place at the boundary of the antiferromagnetic Brillouin zone at point $(\pi/2, \pi/2)$. To construct a spatially homogeneous solution, we choose a linear superposition of covers $K2$ and $K3$. This is attained by averaging the jump matrix that determines reciprocal Green's function (6):

$$T_{\alpha\beta}(\mathbf{k}) = \frac{1}{2}(T^{K2}_{\alpha\beta}(\mathbf{k}) + T^{K3}_{\alpha\beta}(\mathbf{k})), \quad (14)$$

where $\mathbf{k}$ is the wavevector assuming the values in the initial Brillouin zone.

Let us consider this stage in greater detail. Using any cover ($K1$, $K2$, or $K3$), we can introduce the intercluster jump matrix $T_{\alpha\beta}(\tilde{\mathbf{k}})$ (see relation (5)) as a function of wavevector $\tilde{\mathbf{k}}$ defined in the corresponding reduced Brillouin zone. In view of translational symmetry of the reciprocal space, we can write

$$T_{\alpha\beta}(\tilde{\mathbf{k}}) = T_{\alpha\beta}(\tilde{\mathbf{k}} + \mathbf{K}),$$

where $\mathbf{K}$ is the translation vector of the reciprocal space of the superlattice (which is a function of cover). Let $\mathbf{g}_x$ and $\mathbf{g}_y$ be the elementary translation vectors in the reciprocal space of the initial lattice. Then covers $K1$, $K2$, and $K3$ satisfy the following equalities:

$$T^{K1}_{\alpha\beta}(\tilde{\mathbf{k}}) = T^{K1}_{\alpha\beta}(\tilde{\mathbf{k}} + 0.5n\mathbf{g}_x + 0.5m\mathbf{g}_y), \quad (15)$$

$$T^{K2}_{\alpha\beta}(\tilde{\mathbf{k}}) = T^{K2}_{\alpha\beta}(\tilde{\mathbf{k}} + n\mathbf{g}_x + 0.5m\mathbf{g}_y), \quad (16)$$

$$T^{K3}_{\alpha\beta}(\tilde{\mathbf{k}}) = T^{K3}_{\alpha\beta}(\tilde{\mathbf{k}} + 0.5n\mathbf{g}_x + m\mathbf{g}_y), \quad (17)$$

where n and m are integers. Pay attention to the fact that the dependence of Green's function $D_{\alpha\beta}(\tilde{\mathbf{k}}, \omega)$ on the wavevector is determined by jump matrix $T_{\alpha\beta}(\tilde{\mathbf{k}})$ (6); i.e., we can write analogous equalities (15)–(17) for the given Green's function. On the other hand, the Green's function defined by expression (10) must correspond to the symmetry of a square lattice. Using cover $K1$, it is possible to restore the symmetry of the initial square lattice because the corresponding jump matrix is symmetric relative to translations by vectors $\mathbf{g}_x$ and $\mathbf{g}_y$ (the coefficients at integers are identical and equal 0.5). However, jump matrices for covers $K2$ and $K3$ do not exhibit such symmetry; consequently, the use of these covers separately does not yield a correct result.

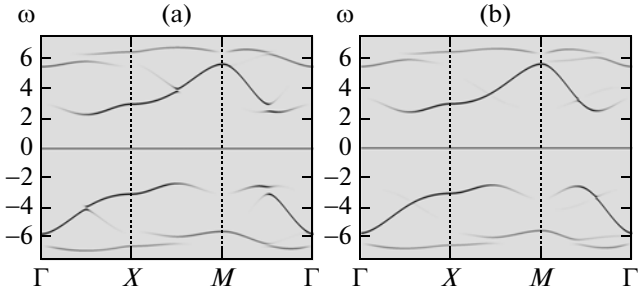

Fig. 2. Dispersion curves for the undoped case ($n_e = 1$) along symmetric direction $\Gamma \longrightarrow X \longrightarrow M \longrightarrow \Gamma$ in the first quadrant of the first Brillouin zone: (a) cover $K1$ and (b) with averaging over two configurations $K2$ and $K3$. The following notation is used: $\Gamma = (0, 0)$, $X = (\pi, 0)$, and $M = (\pi, \pi)$.

Taking into account equalities (16) and (17) and the remarks concerning wavevectors $\mathbf{k}$ and $\tilde{\mathbf{k}}$ following expression (10), we can perform averaging procedure (14) at each point $\mathbf{k}$ of the initial Brillouin zone, which makes it possible to obtain a new jump matrix possessing translational symmetry of the reciprocal space of the initial lattice. This allows us to use formula (6) (with substitution $\tilde{\mathbf{k}} \longrightarrow \mathbf{k}$) for calculating the best approximation of the Green's function in the X representation, which is directly used in expression (10).

It should be noted that after such a procedure, Green's function (6) is defined in the initial Brillouin zone, and Green's function (10) possesses the symmetry of a square lattice. Indeed, the dispersion relation obtained in this way (see Fig. 2b) does not contain a gap and corresponds to the paramagnetic state. We will confine our analysis to the paramagnetic state, which exhibits the short-range antiferromagnetic order due to spin correlations of the first and second neighbors in the cluster. Note that an analogous averaging procedure based on the boundary conditions is often used in studies with exact diagonalization of final clusters [31, 32].

In principle, it is also possible to average a more physical quantity like the spectral function. However, it is much more technically complicated because the entire body of computations in this case should be performed for each cover separately with different sets of poles; i.e., functions $A^{K1}_{\sigma}(\mathbf{k}, \omega)$ and $A^{K2}_{\sigma}(\mathbf{k}, \omega)$ must first be evaluated and then averaged. The advantage of our approach is that averaging is carried out at the initial stage of computation. This allows us to unambiguously determine the poles of the Green's function and their spectral weight for each value of wavevector $\mathbf{k}$ in

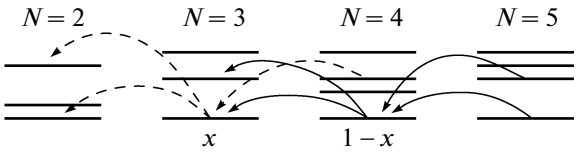

Fig. 3. Diagram of the low-energy part of the Hilbert space for a 2×2 cluster. The probability of filling is $1 - x$ for the ground energy level with $N = 4$ and x for the energy level with $N = 3$. Solid arrows depict annihilation of an electron for zero doping level ($x = 0$), and dashed arrows show additional transitions which must be taken into account in the case of doping ($x \neq 0$); N is the number of electrons in a cluster.

the first Brillouin zone and to substantially reduce the computer time.

Here, we analyze the properties of systems with SECs with various doping levels x, where x is the hole concentration on the cluster. Before we analyze the results, it should be clarified how the doping level is taken into account in the computational algorithm used here. The procedure of exact diagonalization of the Hamiltonian of a 2×2 cluster gives a complete set of eigenvalues and eigenvectors determining the Hilbert space. Figure 3 shows schematically the low-energy part of this space. In the case of half-filling (without doping) and $T = 0$, nonzero filling factor (9) contains transitions between the ground state in the subspace with $N = 4$ and the states in the subspaces with $N = 3$ and $N = 5$ (marked by solid arrows in Fig. 3). In the case of hole (electron) doping, we must take into account the possibility of filling of the ground state in the subspace with $N = 3$ ($N = 5$). As a result, additional transition with a nonzero filling factor appear (marked by dashed arrows in Fig. 3 in the case of hole doping). It should be noted that we consider only one-electron transitions with a change in the number of particles by ± 1. Pay attention to the notation used here. Since the number of sites in the cluster is four in our case, doping to cluster (x) and doping to site (p) are connected by the relation $x = 4p$.

3. GROUND STATE ENERGY

A good verification of the method proposed in the previous section is the comparison of the ground-state energy obtained using the given approach with the results of nonperturbative computations.

Let us calculate the ground state energy confining our analysis only to jumps between the nearest neighbors. In our case, it is convenient to use the following formula for computing the ground state energy per site:

$$E_0 = \frac{1}{2N}\sum_{\sigma \mathbf{k}} \int_{-\infty}^{0} d\omega (\varepsilon_k + \omega + \mu) A_\sigma(\mathbf{k}, \omega) \qquad (18)$$

(the derivation of this formula can be found, for example, in [30, 33]). Here, $\varepsilon_k = -2t(\cos k_x + \cos k_y)$ is the quasiparticle spectrum in the absence of interaction (lattice constant is set as unity); $\mathbf{k}$ is the wavevector assuming its values in the initial Brillouin zone, and N is the number of sites in the initial lattice.

Figure 4a shows the concentration dependences of the ground-state energy per site, calculated by different (including nonperturbative) methods. It can be seen that our result is in good agreement with the

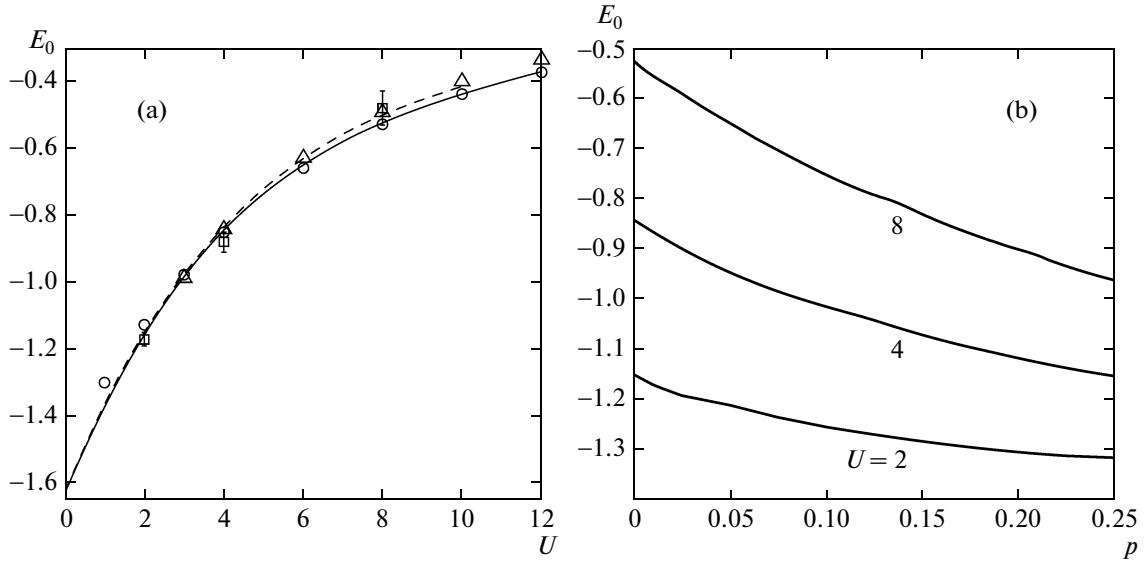

Fig. 4. Dependence of ground-state energy E_0 for zero doping on parameter U (a) and on hole concentration for $U/t = 2$, 4, and 8 (b). Solid curves correspond to the results of our calculation, dot-and-dash curves correspond to variational cluster perturbation theory (V-CPT) [37]; triangles, to the variational Monte Carlo method (VMC) [34], circles, to exact diagonalization (ED) of a 4×4 cluster [36]; squares, to the quantum Monte Carlo method (QMC) [35].

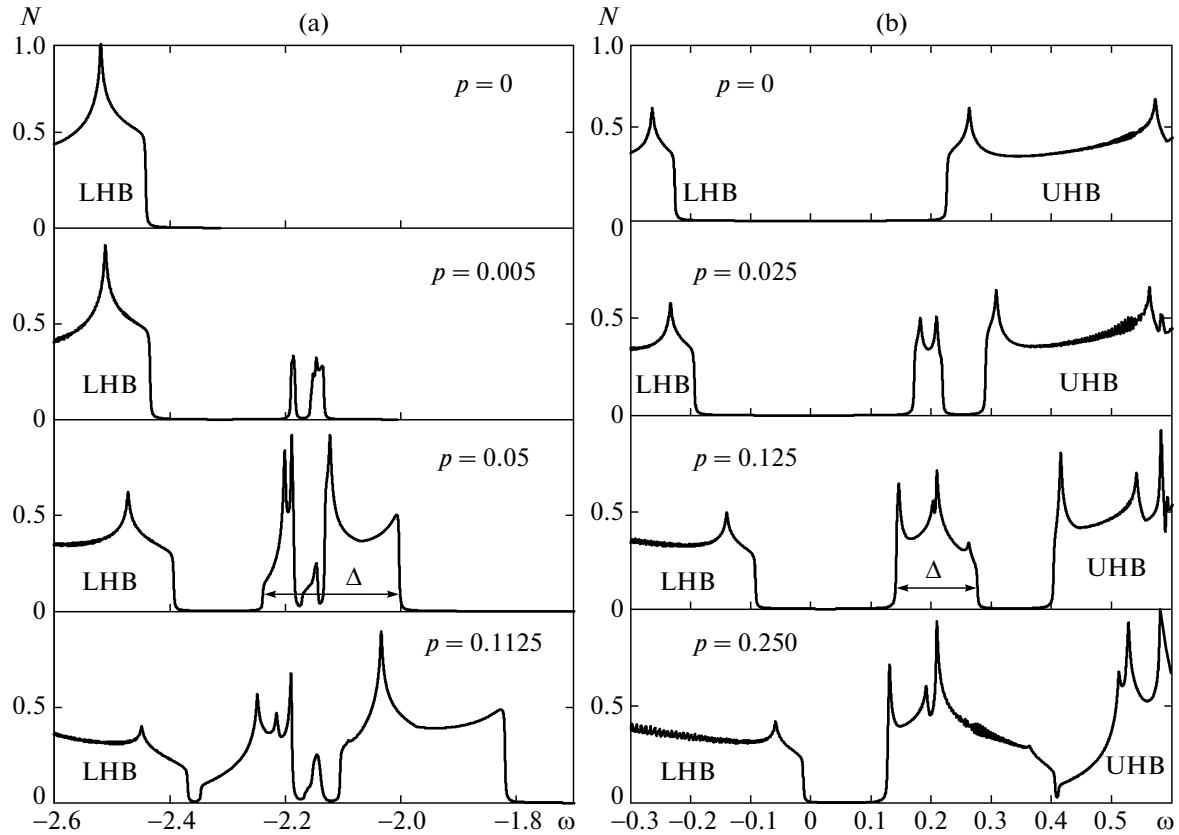

Fig. 5. Density of states near the top of the lower Hubbard band (LHB), the bottom of the upper Hubbard band (UHB), and of the in-gap states. The hole concentration is indicated in the figure. Model parameters: $U = 8t$ (a), $U = 2t$ (b), and $t' = t'' = 0$; the Lorentzian halfwidth is $\delta = 0.001t$; Δ is the bandwidth for the in-gap states.

results obtained by the variational and quantum Monte Carlo methods [34, 35]. Excellent agreement is observed with the results of calculations by the exact diagonalization method for the 4 × 4 cluster [36]. Comparison of our calculations with the results obtained in [37] based on the cluster perturbation theory supplemented with a variational procedure shows good agreement for small U and provides the best result in the remaining range of values.

We supplement analysis of the ground-state energy by tracing its dependence on the doping level. Figure 4b shows the dependences of the ground state energy per cite, E_0, on the doping level for three values of parameter $U/t = 2$, 4, and 8. It can be seen that with increasing concentration of holes to a doping level of 25%, the value of E_0 decreases for all values of U. This variation occurs more slowly for smaller values of U. The energy value in this case increases with the Coulomb repulsion parameter.

4. IN-GAP STATES

Analysis of systems with SECs revealed that doping affects the energy band in the whole and requires the rejection of the "hard band" concept. It was found, in particular, that doping leads to the formation of in-gap states [38]. In this section, we report on the results of analysis of these states using the cluster approach and taking into account jumps t only between the nearest neighbors. All energies will be given below in the units of t with a shift by $U/2$.

Information on the band structure can be obtained from analysis of the density of states. As expected, in the limit of zero doping level, splitting of the band into the lower and upper Hubbard bands (LHB and UPB, respectively) is observed. Upon an increase in the hole concentration, a rearrangement of the two subbands takes place with the formation of in-gaps states between them. It is clear from Fig. 5 that an insignificant concentration leads to the formation of in-gap states near the top of the LHB at $U = 8$. Analogous states also appear near the bottom of the UHB at $U = 2$. A further increase in the concentration leads to an increase in the spectral intensity and to a broadening of the band of these states. Calculations show that at $U > U_1 \approx 3.5$, the in-gap states are localized near the top of the LHB, while in the range $U_0 < U < U_1$, such states are localized near the bottom of the UHB. Here, we have determined the lower limit of U for the existence on in-gap states, $U_0 \approx 1.5$, below which such states are

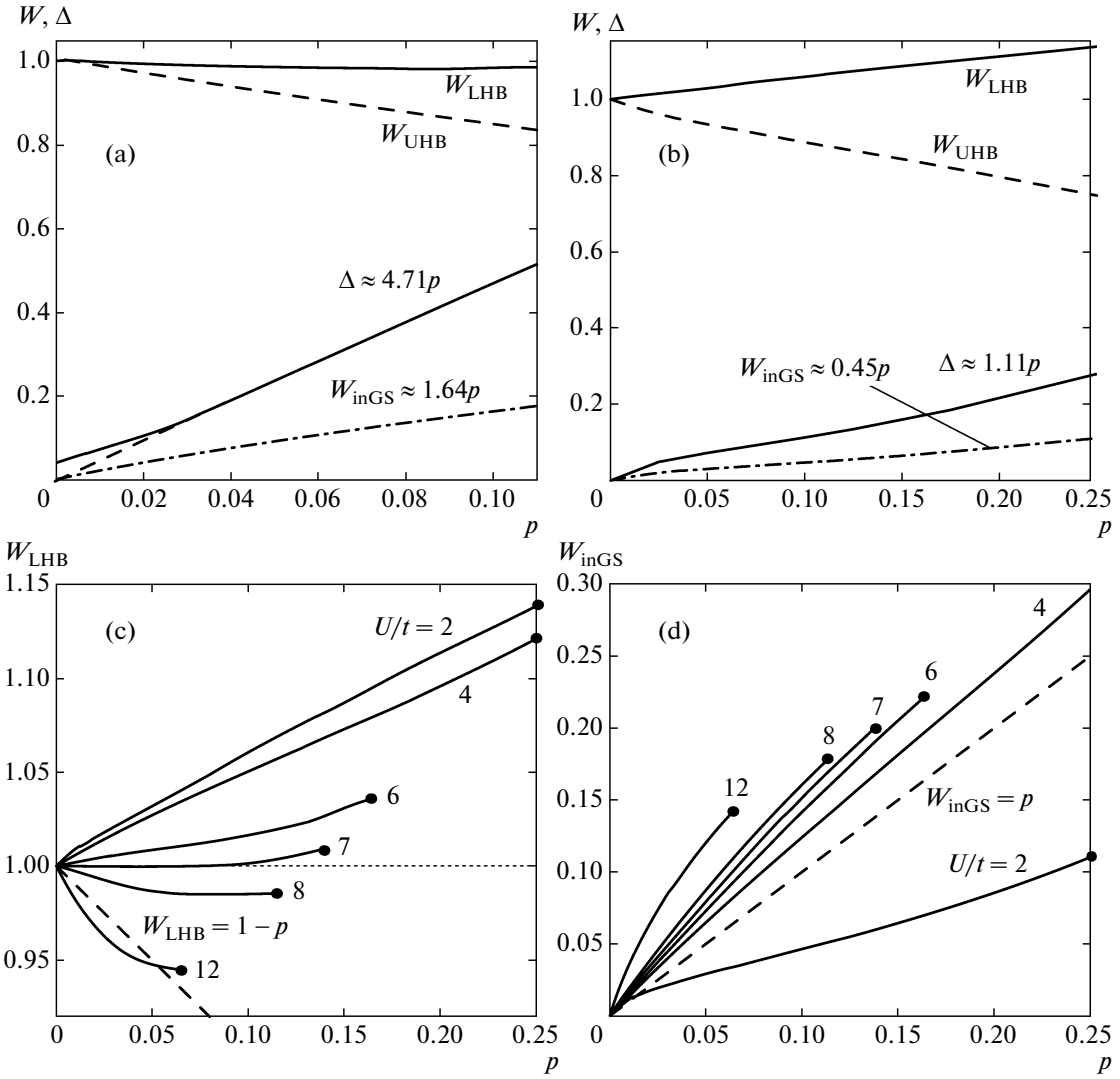

Fig. 6. Dependences of total spectral weight W of the lower Hubbard band (LHB), upper Hubbard band (UHB), the band of in-gap states (inGS), and bandwidth Δ of the in-gap states on the hole doping level. Model parameters: $U = 8t$ (a), $U = 2t$ (b), and $t' = t'' = 0$. Dependences of the total spectral weight W_{LHB} of the lower Hubbard band (c) and spectral weight W_{inGS} of the band of in-gap states (d) on doping level p for various values of parameter U/t. Dots show the maximal doping level at which the Hubbard band merges with the band of in-gap states. Dashed lines are required for analysis of the results.

not observed. This is explained by merging these states with the UHB for any doping level (see below).

The dependence of the total spectral weight W_{inGS} of in-gap band on the doping level reveals a monotonic increase for various values of Coulomb parameter U (see Fig. 6). It can be seen from Fig. 6a that for $U = 8$, the spectral weight W_{UHB} of the UHB decreases with increasing doping level in accordance with variation in W_{inGS}. It can be stated that the spectral "flows" from the UHB to the band with in-gap states. Figure 6b shows analogous dependences for $U = 2$. However, a considerable difference in the concentration dependence of W_{LHB} is observed. In the latter case, the total weight of the LHB noticeably increases with the doping level. On the whole, the spectral weight flows from the UHB to LHB and into in-gap states. Figure 6a and 6b show the numerical values of the rate of increase in total spectral weight W_{inGS} and the concentration dependence of bandwidth Δ of in-gap states. The values of these quantities at $U = 8$ are approximately four times higher than the corresponding values at $U = 2$. This difference strongly affects the concentration range in which the in-gap states can be determined rigorously. For this reason, the dependence of the spectral weights was traced only to values of $p = 0.11$ at $U = 8$ and $p = 0.25$ at $U = 2$ because a further increase in concentration leads to merging of the in-gap states with the Hubbard band and to the formation of the single band. It should be noted in this connection that for $U = 8$, such a merging occurs with the LHB, while for $U = 2$, the in-gap states merge with the UHB.

Analysis of the distribution of the spectral weight among the Hubbard bands and in-gap states revealed an interesting peculiarity. Figure 6 shows only the curves describing the total spectral weight in the LHB (Fig. 6c) and in the band on in-gap states (Fig. 6d) as functions of the doping level for various values of U. The above analysis shows that functions $W_{\mathrm{LHB}}(p)$ and $W_{\mathrm{inGS}}(p)$ cannot be determined for the entire concentration range; for this reason, the curves terminate at bold dots. It can be seen that the variation of Coulomb repulsion parameter U leads to a substantial variation of function $W_{\mathrm{LHB}}(p)$. The value of W_{LHB} decreases upon an increase in the hole concentration for $U >$ 7and increases for $U < 7$. The dependence corresponding to $U = 12$ deserves special attention (Fig. 6c). It can be seen that the major part of this curve lies under the dashed line corresponding to function $W_{\mathrm{LHB}} = 1 - p$ determining the lower value of the density of states required for populating of the LHB with all electrons. This means that the number of states in the LHB is insufficient for populating all electrons of the system; therefore, a part of electrons populate in-gap states. According to calculations, the number of states in the band of in-gap states is large enough for that (see Fig. 6d), which is clear from the comparison with function $W_{\mathrm{inGS}} = p$ (dashed line). Thus, for $U = 12$, the Fermi level in the range of weak doping falls into the band of in-gap states (Fermi level pinning). It should be noted that for lower values of U, the Fermi level lies in the LHB in the entire doping range. An analogous pinning of the Fermi level due to a redistribution of the spectral weight among the band is also observed using cover $K1$ [39].

5. REARRANGEMENT OF THE FERMI SURFACE

Let us now analyze the Fermi surface for various hole doping levels. In this section, we confine our analysis to the Hubbard model with following parameters: $U = 8t$ and $t' = t'' = 0$. Note that in the course of calculations, we controlled the value of the f-factor so that the condition $f > 0.995$ was satisfied for all results considered below. Recent experimental studies have revealed two main features in the behavior of the Fermi state depending on the concentration in high-T_c superconducting materials. These are the change in the topology and the nonuniform redistribution of the spectral weight of quasiparticles over the Fermi state. Such a behavior is primarily associated with the existence of short-range magnetic order. The cluster approach makes it possible to directly take into account this order and to estimate its effect on the quasiparticle spectrum.

Before we analyze the results, the following remarks are due. In view of the approximation used here, we obtain quasiparticles with an infinitely long lifetime, which does not allow us to estimate the broadening of the spectral lines. Nevertheless, line broadening appears in numerical calculations when the delta-function is replaced by the Lorentzian with a preset halfwidth. In this section, the Lorentzian halfwidth is $\delta = 0.1t$. Such a choice is dictated primarily by the desire to match the results of theoretical calculations with experimental ARPES data. In calculating the spectral weight of quasiparticles on the Fermi state, we took into account the contribution from the states in the range of $\pm 0.2t$ from the Fermi level, which is also associated with the technique of ARPES experiments. The typical energy resolution in the ARPES techniques is 10–45 eV [7, 40–42], while the fitting value of the hopping parameter for the nearest neighbors in the tight binding method is $t = 0.25$–0.40 eV [7, 43, 44]. Therefore, the value of the broadening parameter usually varies from $0.02t$ to $0.15t$ [14, 19]. For example, the ARPES results presented in [7] were obtained with a resolution of $\delta = 0.02$ eV, and parameter t was fitted to a value of 0.25 eV. This gives $\delta = 0.08t$. Here, we use typical values of broadening parameter δ. The true linewidth in ARPES is determined not only by the resolution in the energy and wavevector, but also by dynamic processes. The simulation of these processes by the Lorentzian width is too simplified and can be treated only as qualitative. For this reason, we do not consider specific experimental spectra, confining ourselves to model calculations.

Figure 7 shows the evolution of the density of states and Fermi state upon variation in the hole concentration. First, it is clearly seen that the spectral weight distribution over the Fermi state is nonuniform and depends on the doping level (see Figs. 7b–7e). For some values of the hole concentration, the Fermi state has an arc structure. For a doping level of about 22%, the Fermi state topology is transformed, and a transition from a conditionally "hole" pocket (see below) at point (π, π) to an electron pocket at point (0, 0) takes place. These facts indicate that in the range of strong doping, the electron system exhibits a transition to the Fermi-liquid behavior. Simultaneously with the Fermi state evolution, we can observe the behavior of the density of states at the Fermi level (see Fig. 7a). It can be seen that at a doping level of 8%, the Fermi level falls into the region with a lowered density of states (pseudogap) and remains in this region up to a doping level of 22%. The Fermi level attains the minim density of states for a doping level of 13%. In this concentration range, the distribution of the spectral weight over the Fermi state is nonuniform.

If we now disregard the available experimental accuracy and simulate the decrease in the linewidth, we can obtain a more comprehensive pattern of Fermi state variations occurring in the same concentration range. Let us consider the Fermi state evolution for a lower value of the Lorentzian half-width ($\delta = 0.01t$) and reduce the range of states being taken into account near the Fermi level to $\pm 0.02t$. It turns out that with such a resolution, the density of states has a larger number of singularities, and the Fermi state evolution

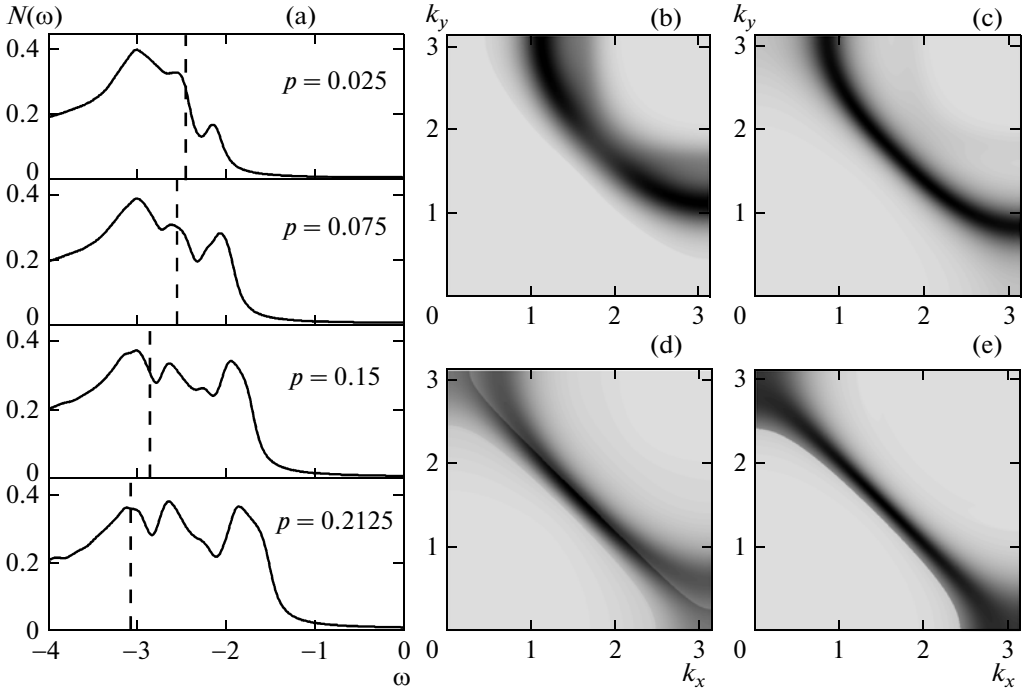

Fig. 7. (a) Density of states near the top of the lower Hubbard band and (b–e) Fermi surface obtained from the distribution of spectral weight of electrons. Hole doping level is $p = 0.025$ (b), 0.075 (c), 0.15 (d), and 0.2125 (e). Vertical straight line in (a) marks the position of the Fermi level. Model parameters: $U = 8t$, $t' = t'' = 0$, and Lorentzian half-width $\delta = 0.1t$.

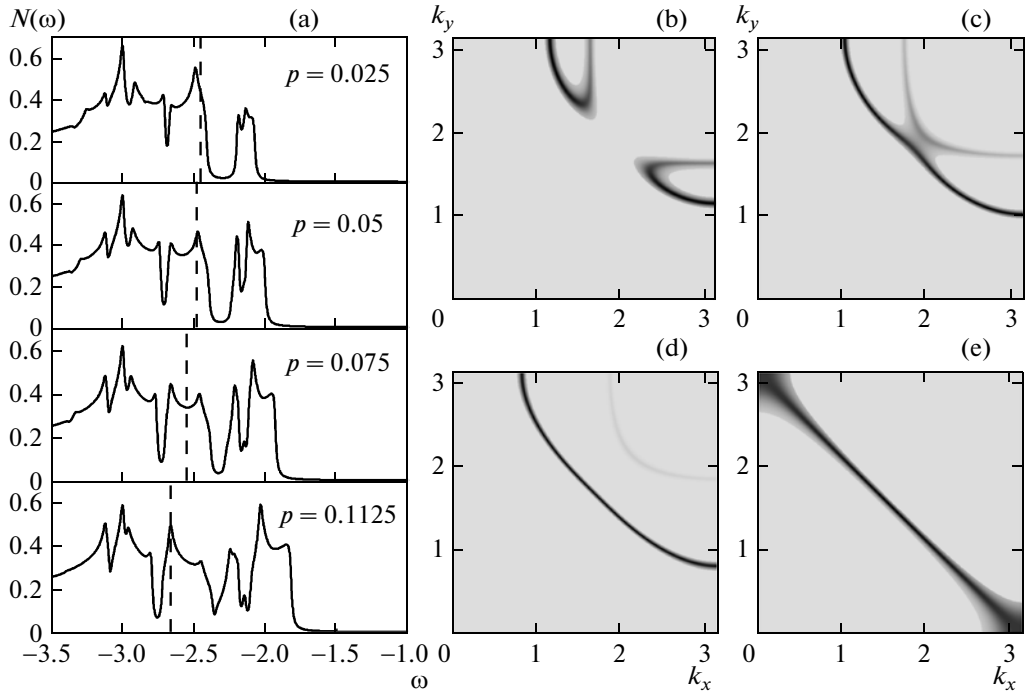

Fig. 8. Same as in Fig. 7 for $p = 0.025$ (b), 0.05 (c), 0.075 (d), and 0.1125 (e) and Lorentzian halfwidth $\delta = 0.01t$.

upon a change in the doping level occurs in a more complex way, which is manifested in a sequence of topological variations (Fig. 8). It can be seen from the density of states that upon an increase in the doping level, the Fermi level passes through two Van Hove singularities and falls into the first pseudogap. Figures 8b–8e show

the FSs with a spectral weight distribution for the same values of concentration as in Fig. 8a; therefore, the conformity of the Van Hove singularities and topological rearrangements of the Fermi state can be easily seen. It is clear that with the resolution adopted here, regions on the Fermi state with a weak spectral weight appear, supplementing information on the total Fermi state. The concept of the simple hole pocket near point (π, π) is obviously not realized for these parameters. In the case of ultraweak doping, we observe hole pockets in the antinodal direction $((\pi, 0) \longrightarrow (\pi, \pi)$, $(0, \pi) \longrightarrow (\pi, \pi))$, which merge for a certain concentration at the point of nodal direction $((0, 0) \longrightarrow (\pi, \pi))$, forming a more complex topology of two surfaces. This variation in the topology is manifested in the density of states in the form of the first Van Hove singularity. The surface with a weak spectral weight forms an electron pocket around point (π, π). Upon an increase in the hole concentration, the surface with a large weakly nonuniform distribution of spectral weights experiences another topological transformation. This leads to the formation of an electron pocket around point (0, 0). Accordingly, this variation in the Fermi state topology is manifested in the density of states in the form of the second Van Hove singularity.

Concluding this section, we emphasize that the singularities revealed above appear due to the existence of the short-range magnetic order in the system, which is directly taken into account in the cluster approach.

6. EFFECT OF DISTANT JUMPS

For a more complete comparison with real cuprates, we must take into account the effect of jumps between distant neighbors. In most theoretical publications, the authors confine analysis to jumps up to the third neighbor inclusively because the allowance for more distant jumps leads to insignificant corrections. Let us consider the effect of jumps between the second and third nearest neighbors using the cluster approach described above. In our choice of model parameters, we use the results of calculations performed in [12] for the LSCO system. The set of parameters is as follows: $U = 4$ eV, $t = 0.93$ eV, $t' = 0.12$ eV, and $t'' = 0.15$ eV. In our calculations, we use parameters normalized to t: $U = 4.3$ eV, $t' = -0.13$ eV, and $t'' = 0.16$ eV. It should be noted that in the case of a 2×2 cluster, the jumps between the first and second nearest neighbors are taken into account even in calculation of the eigenstates of the cluster, while the jumps between the third nearest neighbors are taken into account only in the interaction between clusters.

It should be noted that for systems with SECs, the Green's function has not only poles, but also zeros. This result was obtained using the CDMFT + ED method [14, 45]. In our calculations, the structure of poles and zeros, which coincides qualitatively with the results of [45], is also reproduced (Figs. 9a, 9d, and 9g). The sequence of the changes in the Fermi surface topology is the same as that obtained earlier in [10, 12]. The maps of spectral weight distribution $A(\mathbf{k}, \varepsilon_F)$ in the limit $\delta \longrightarrow 0$ must generally give the same pattern of the Fermi surface as that obtained from analysis of the dispersion relations. Indeed, comparison of the data from the first and second columns in Fig. 9 gives an analogous pattern. The maps of the spectral weight also show its nonuniform distribution in the Brillouin zone. Similar regions with a small spectral weight have been obtained earlier in [10]. However, the contemporary resolution level in the ARPES spectra corresponds not to the second column ($\delta = 0.01$), but also the third column ($\delta = 0.1$) in Fig. 9. The broadening that appears as a result is so strong that a small pocket is "washed off" into the arc (Fig. 9c). Instead of two concentric pockets around point (π, π) in the intermediate concentration range, strong broadening also gives an arc (Fig. 9f). The pattern following from ARPES corresponds to the Fermi surface only in the range of high concentrations, in which only one large surface is left (Figs. 9g–9i). It should be noted that in spite of the qualitative similarity of the evolution of the Fermi surface upon doping and the results of earlier works [12], the numerical values of the critical concentrations for the Lifshitz transitions do not coincides. These values obviously depend on the type of the model (spin-fermion model [10], Hubbard model [11], and t–J model [12]) and on the numerical values of the model parameters.

The presence of a pseudogap in the vicinity of the antinodal point $(\pi, 0)$ and its gradual occlusion upon an increase in the concentration is illustrated in Fig. 10. The arc length measured in ARPES is small in the doping range $p \leq 0.05$ and gradually increases with p. The constancy of the spectral weight on the Fermi surface at $p = 0.25$ corresponds to the expected Fermi-liquid behavior.

The in-gap states for $U = 4.3t$ lie near the LHB and have the largest spectral weight in the vicinity of point $M = (\pi, \pi)$ (Fig. 11).

The dispersion dependence along symmetric direction $\Gamma \longrightarrow X \longrightarrow M \longrightarrow \Gamma$ agrees well with the results of other publications [19, 46] (see Fig. 11). In particular, the saddle singularity with a large spectral weight observed in the vicinity of point X is in good agreement with ARPES experiments. Analysis of dispersion along the nodal direction has revealed segments with different slopes on the dispersion curves. For a broadening of $\delta = 0.1t$, this singularity is more clearly pronounced for a large parameter U. It should be noted that such a distortion of the dispersion curve strongly resembles the kinks observed in numerous experiments [13–16]. An increase in the resolving power (i.e., a decrease in δ) has made it possible to distinguish segments with different slopes on the dispersion curve, which are separated from one another by gaps (Fig. 11c). Analysis of the results shows that with increasing Coulomb repulsion parameter U, these

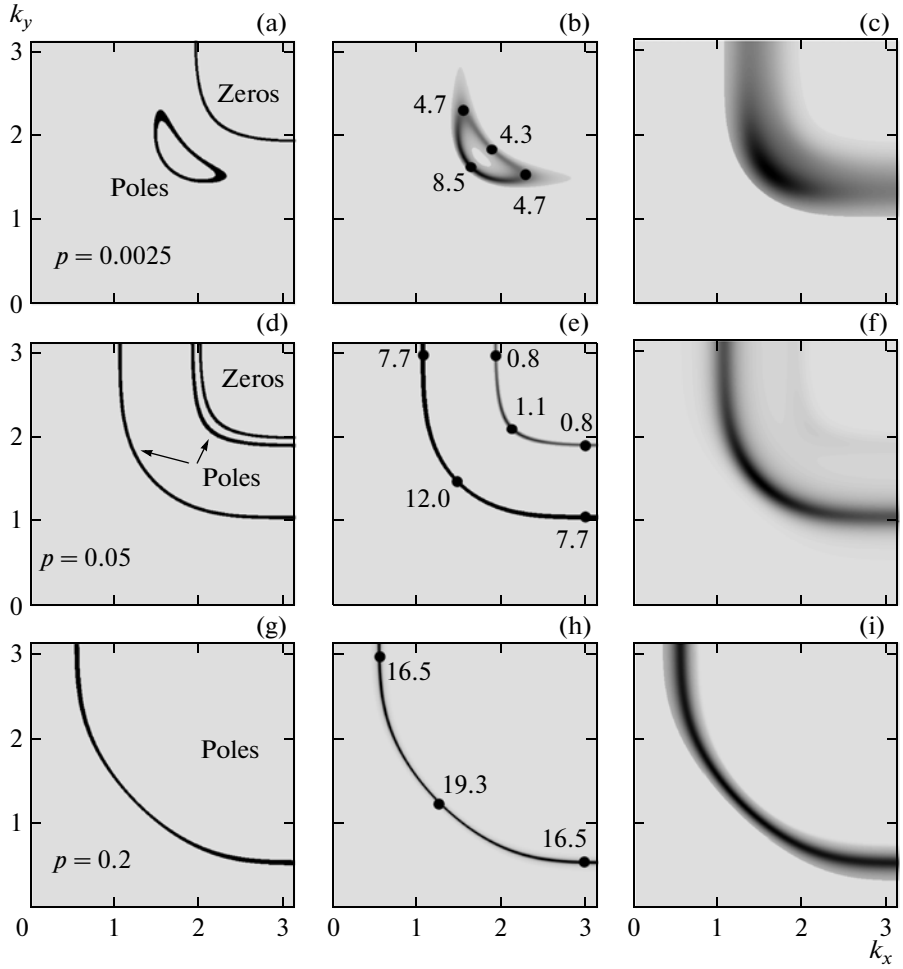

Fig. 9. Concentration dependences of the Fermi surface (a, d, g) and spectral weight maps for different broadening levels $\delta = 0.01t$ (b, e, h) and $\delta = 0.1t$ (c, f, i). Numbers on maps (b, e, h) indicate a nonuniform distribution of the spectral weight. Model parameters: $U = 4.3t$, $t' = -0.13t$, and $t'' = 0.16t$.

gaps become broader. The electronic mechanism of kink formation has been observed earlier in [18].

Using the results obtained in [47], we considered another set of model parameters for LSCO: $U = 4.65t$, $t' = -0.17t$, and $t'' = 0.085t$. On the hole, the behavior of the main characteristics of the electron system is similar to that described above (for parameter $U = 4.3$). A significant distinction is the absence of a hole pocket in the nodal direction for low hole concentrations. In this case, evolution of the Fermi state begins with splitting of the arc and the formation of a structure similar to that depicted in Fig. 9e. Analysis shows that the existence of a hole pocket in the nodal direction depends on the value of hopping t'' to the third nearest neighbors. An increase in this parameter leads to stabilization of the Fermi state pocket.

Generalizing our results, we can draw the following conclusion. For linewidth $\delta = 0.1t$, the spectral intensity distribution over the Brillouin zone, which is observed in ARPES, does not provide a comprehensive answer to the question about the true topology of the Fermi surface in HTSC cuprates. Only an order-of-magnitude decrease in the linewidth makes it possible to obtain the true Fermi surface from the spectral intensity distribution.

7. DISCUSSION OF RESULTS

Let us summarize our results. Comparison with the results of other theoretical and experimental works shows good agreement in a number of common characteristic features of systems with SECs. First, this is the existence of in-gap states in a wide range of doping. Our calculations show that the spectral weight of the in-gap band increases with the hole concentration mainly due to the spectral weight of the upper Hubbard band (see Fig. 6). We have revealed a dependence of the position of in-gap states on Coulomb repulsion parameter U. In particular, these states appear near the lower Hubbard band for $U = 8$ and near the upper Hubbard band for $U = 2$. A difference in the spectral intensity distributions also exists. In the former case,

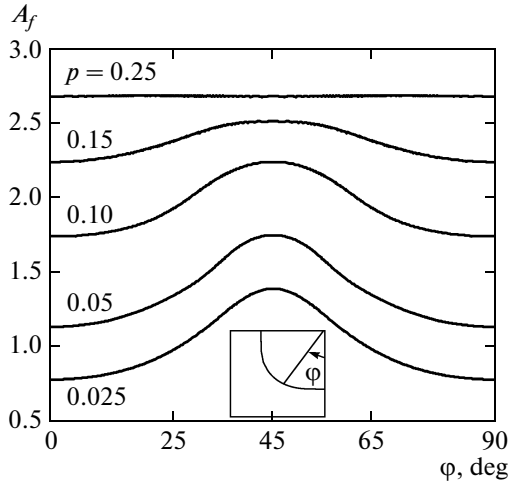

Fig. 10. Dependences of spectral intensity A_f on the Fermi surface on angle φ for various doping levels. Here, φ = 0 corresponds to the antinodal direction ((π, 0) ⟶ (π, π)) and φ = 45° corresponds to the nodal direction ((0, 0) ⟶ (π, π)). Model parameters: $U = 2.15t$, $t' = -0.13t$, and $t'' = 0.16t$; $\delta = 0.1t$.

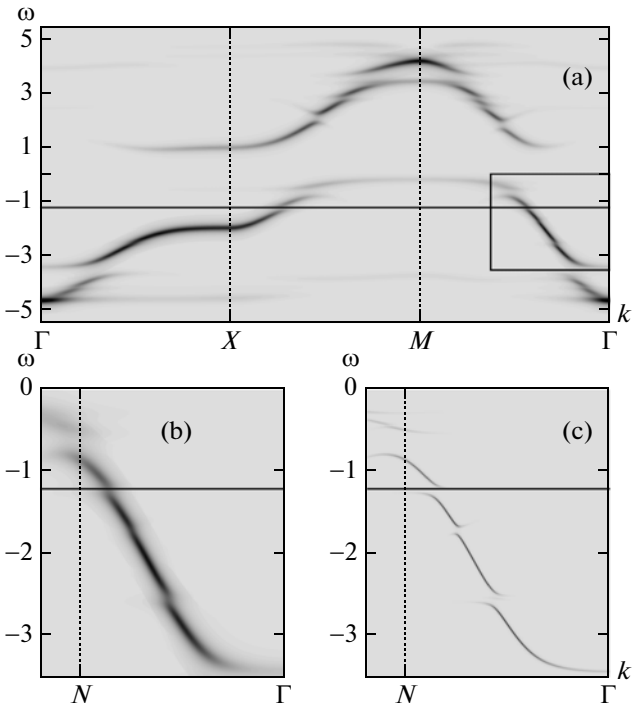

Fig. 11. (a) Dispersion curves along symmetric direction Γ ⟶ X ⟶ M ⟶ Γ in the first quadrant of the first Brillouin zone and (b, c) framed nodal domain at a doping level of 10% and $U = 4.3t$, $t' = -0.13t$, and $t'' = 0.16t$. Horizontal solid line indicates the position of the Fermi level. Lorentzian halfwidth is $\delta = 0.1t$ (b) and $\delta = 0.01t$ (c). The following notation is used: Γ = (0, 0), X = (π, 0), M = (π, π), and N = (π/2, π/2).

the spectral weight differs from zero for quasiparticles near point M, and in the latter case, near points X and N. Analogous behavior is also observed for other model parameters.

Our analysis reveals that spectral weight W_{LHB} of the LHB also depends on the concentration and Coulomb repulsion parameter U (see Fig. 6). Upon an increase in this parameter, the behavior of the system changes significantly. For $U = 7$, a change in functional dependence $W_{\mathrm{LHB}}(p)$ is observed, while for $U =$ 12, spectral weight W_{LHB} in the low doping range decreases so strongly that the number of states in the LHB becomes smaller than the total number of electrons in the system. As a result, the Fermi level falls into the region of in-gap states.

In this study, we have observed pseudogap states and a nonuniform distribution of the spectral weight of quasiparticles over the Femi surface. Our calculations revealed a cascade of quantum phase transitions upon an increase in the hole concentration, which could be observed only with a high resolution (see Fig. 9) (we mean the energy resolution in ARPES experiments). In our calculations, the role of this quantity was played by Lorentzian halfwidth δ, which is convenient for simulating the theoretical calculation. It should be noted that only qualitative comparison with ARPES data was carried out.

In the case of nonzero distant jumps, we obtained the Fermi surface in the form of an arc (see Figs. 9c, 9f, and 9i), which conforms with ARPES data [9, 48]. We revealed one more part of the Fermi surface with a very small spectral weight (Fig. 9e), as well as zeros of the Green's function in the low-doping range, which correspond to the results obtained using the CDMFT + ED method [14]. For a certain set of model parameters, a small pocket in the nodal direction was observed on the Fermi level in the range of ultralow doping (see Figs. 9a and 9b). Analysis of the results obtained with different resolutions has made it possible to estimate the role of resolution in ARPES experiments in analysis of the dependence of the Fermi surface behavior on the hole concentration. We hope that future experiments with a better resolution will reveal a finer energy structure of the electron system in materials with SECs.

Small hole pockets in the range of weakly doped cuprates were observed experimentally in measuring Landau quantum oscillations in strong magnetic fields [9]. The fact that the pockets are blurred into arcs upon line broadening was noted by many authors (see [14, 18]). We have proved that broadening blurs the pattern of the Lifshitz transitions and leads to smooth occlusion of the pseudogap (see Fig. 10).

The dispersion dependences along symmetric directions (Fig. 11) are in good agreement with the results of other studies (in particular, with study [19] carried out using the cluster generalization of the dynamic mean field theory). A number of publications are devoted to analyzing the variation in the slope of

the dispersion curve below the Fermi level (kinks). Several types of kinks have been revealed [49, 50]. We have demonstrated in this study that the dispersion curve splits in the nodal direction into segments with different slopes separated by gaps (see Fig. 11). Since we have disregarded the phonon component in the approach used here, the difference in the slopes is associated with the direct interaction in the electron subsystem. Thus, the experimentally observed kinks can be a consequence of electron–electron interactions leading to a distortion of the dispersion curve. This conclusion agrees with the results obtained in [50].

It should be noted that our results were obtained using the cluster approach, in which the short-range order can be taken into account exactly. We used the technique of the Hubbard X operators, which allowed us to introduce the quantity (f-factor) ensuring control over the total spectral weight of quasiparticles within the required accuracy limits. The calculated values of the ground-state energy (see Fig. 4) and all other results confirm the validity of the approach used here for analyzing systems with strong electron correlations. Preliminary results of this study were published in [51].

ACKNOWLEDGMENTS

The authors thank V.V. Valkov for helpful discussions of the results.

This study was supported financially by the Russian Foundation for Basic Research (project nos. 10-02-90725-mob_st and 09-02-00127), Program 18.7 of the Presidium of the Russian Academy of Sciences, the Federal Target Program "Personnel" (state contract no. P891), and the integrated project no. 40 of the Siberian Branch of the Russian Academy of Sciences.

REFERENCES

1. O. Fischer, M. Kugler, I. Maggio-Aprile, C. Berthod, and C. Renner, Rev. Mod. Phys. **79**, 353 (2007).
2. A. Damascelli, Z. Hussain, and Z. Shen, Rev. Mod. Phys. **75**, 473 (2003).
3. M. V. Sadovskii, Phys.—Usp. **44** (5), 515 (2001).
4. A. Kanigel, M. R. Norman, M. Randeria, U. Chatterjee, S. Souma, A. Kaminski, H. M. Fretwell, S. Rosenkranz, M. Shi, T. Sato, T. Takahashi, Z. Z. Li, H. Raffy, K. Kadowaki, D. Hinks, L. Ozyuzer, and J. C. Campuzano, Nat. Phys. **2**, 447 (2006).
5. K.-Y. Yang, T. M. Rice, and F.-C. Zhang, Phys. Rev. B: Condens. Matter **73**, 174501 (2006).
6. P. A. Lee, N. Nagaosa, and X.-G. Wen, Rev. Mod. Phys. **78**, 17 (2006).
7. T. Yoshida, X. J. Zhou, D. H. Lu, S. Komiya, Y. Ando, H. Eisaki, T. Kakeshita, S. Uchida, Z. Hussain, Z.-X. Shen, and A. Fujimori, J. Phys.: Condens. Matter **19**, 125209 (2007).
8. M. Hashimoto, T. Yoshida, H. Yagi, M. Takizawa, A. Fujimori, M. Kubota, K. Ono, K. Tanaka, D. H. Lu, Z.-X. Shen, S. Ono, and Y. Ando, Phys. Rev. B: Condens. Matter **77**, 094516 (2008).
9. N. Doiron-Leyrand, C. Proust, D. LeBoeuf, J. Levallois, J.-B. Bonnemaison, R. Liang, D. A. Bonn, W. N. Hardy, and L. Taillefer, Nature (London) **447**, 565 (2007).
10. A. F. Barabanov, A. A. Kovalev, O. V. Urazaev, A. M. Belemuk, and R. Hayn, JETP **92** (4), 677 (2001).
11. N. M. Plakida and V. S. Oudovenko, JETP **104** (2), 230 (2007).
12. M. M. Korshunov and S. G. Ovchinnikov, Eur. Phys. J. B **57**, 271 (2007).
13. A. F. Barabanov and A. M. Belemuk, JETP **111** (2), 258 (2010).
14. S. Sakai, Y. Motome, and M. Imada, Phys. Rev. Lett. **102**, 056404 (2009).
15. S. G. Ovchinnikov, M. M. Korshunov, and E. I. Shneyder, JETP **109** (5), 775 (2009).
16. S. V. Borisenko, A. A. Kordyuk, V. Zabolotnyy, J. Geck, D. Inosov, A. Koitzsch, J. Fink, M. Knupfer, B. Büchner, V. Hinkov, C. T. Lin, B. Keimer, T. Wolf, S. G. Chiuzbâian, L. Patthey, and R. Follath, Phys. Rev. Lett. **96**, 117004 (2006).
17. A. Lanzara, P. V. Bogdanov, X. J. Zhou, S. A. Kellar, D. L. Feng, E. D. Lu, T. Yoshida, H. Eisaki, A. Fujimori, K. Kishio, J.-I. Shimoyama, T. Noda, S. Uchida, Z. Hussain, and Z.-X. Shen, Nature (London) **412**, 510 (2001).
18. E. Z. Kuchinskii, I. A. Nekrasov, and M. V. Sadovskii, JETP Lett. **82** (4), 198 (2005).
19. M. Civelli, Phys. Rev. B: Condens. Matter **79**, 195113 (2009).
20. T. Maier, M. Jarrell, T. Pruschke, and M. H. Hettler, Rev. Mod. Phys. **77**, 1027 (2005).
21. A. F. Barabanov, L. A. Maksimov, and A. V. Mikheenkov, Sov. Phys. Solid State **30** (8), 1449 (1988).
22. A. F. Barabanov, L. A. Maksimov, and A. V. Mikheyenkov, J. Phys.: Condens. Matter **1**, 10143 (1989).
23. S. G. Ovchinnikov and I. S. Sandalov, Physica C (Amsterdam) **161**, 607 (1989).
24. J. Hubbard, Proc. R. Soc. London, Ser. A **276**, 238 (1963).
25. J. Hubbard, Proc. R. Soc. London, Ser. A **285**, 542 (1965).
26. S. V. Nikolaev and S. G. Ovchinnikov, JETP **111** (4), 635 (2010).
27. V. V. Val'kov and S. G. Ovchinnikov, *Quasiparticles in Strongly Correlated Systems* (Siberian Branch of the Russian Academy of Sciences, Novosibirsk, 2001) [in Russian].
28. R. O. Zaitsev, Sov. Phys. JETP **41** (1), 100 (1975).
29. R. O. Zaitsev, *Diagrammatic Method in the Theory: Superconductivity and Ferromagnetism* (Editorial URSS, Moscow, 2004; KomKniga, Moscow, 2007).
30. D. Senechal, D. Perez, and D. Plouffe, Phys. Rev. B: Condens. Matter **66**, 075129 (2002).
31. D. Poilblanc, Phys. Rev. B: Condens. Matter **44**, 9562 (1991).

32. T. Tohyama, Phys. Rev. B: Condens. Matter **70**, 174517 (2004).
33. C. Kittel, *Quantum Theory of Solids* (Wiley, New York, 1963; Nauka, Moscow, 1967).
34. H. Yokoyama and H. Shiba, J. Phys. Soc. Jpn. **56**, 3582 (1987).
35. J. E. Hirsch, Phys. Rev. B: Condens. Matter **31**, 4403 (1985).
36. G. Fano, F. Ortolani, and A. Parola, Phys. Rev. B: Condens. Matter **42**, 6877 (1990).
37. C. Dahnken, M. Aichhorn, W. Hanke, E. Arrigoni, and M. Potthoff, Phys. Rev. B: Condens. Matter **70**, 245110 (2004).
38. S. G. Ovchinnikov, Sov. Phys. JETP **75** (2), 283 (1992).
39. S. V. Nikolaev and S. G. Ovchinnikov, Zh. Sib. Fed. Univ., Mat. Fiz. **4**, 162 (2011).
40. D. S. Marshall, D. S. Dessau, A. G. Loeser, C-H. Park, A. Y. Matsuura, J. N. Eckstein, I. Bozovic, P. Fournier, A. Kapitulnik, W. E. Spicer, and Z.-X. Shen, Phys. Rev. Lett. **76**, 4841 (1996).
41. A. Ino, C. Kim, M. Nakamura, T. Yoshida, T. Mizokawa, Z.-X. Shen, A. Fujimori, T. Kakeshita, H. Eisaki, and S. Uchida, Phys. Rev. B: Condens. Matter **62**, 4137 (2000).
42. T. Yoshida, M. Hashimoto, T. Takizawa, A. Fujimori, M. Kubota, K. Ono, and H. Eisaki, Phys. Rev. B: Condens. Matter **82**, 085119 (2010).
43. A. A. Kordyuk, S. V. Borisenko, M. Knupfer, and J. Fink, Phys. Rev. B: Condens. Matter **67**, 064504 (2003).
44. W. Prestel, F. Venturini, B. Muschler, I. Tütto, R. Hackl, M. Lambacher, A. Erb, S. Komiya, S. Ono, and Y. Ando, D. Inosov, V. B. Zabolotnyy, and S. V. Borisenko, Eur. Phys. J.: Spec. Top. **188**, 163 (2010).
45. T. D. Stanescu and G. Kotliar, Phys. Rev. B: Condens. Matter **74**, 125110 (2006).
46. A.-M. S. Tremblay, B. Kyung, and D. Senechal, Low Temp. Phys. **32** (4), 424 (2006).
47. E. Pavarini, I. Dasgupta, T. Saha-Dasgupta, O. Jepsen, and O. K. Andersen, Phys. Rev. Lett. **87**, 047003 (2001).
48. T. Yoshida, M. Hashimoto, S. Ideta, A. Fujimori, K. Tanaka, N. Mannella, Z. Hussain, Z.-X. Shen, M. Kubota, K. Ono, S. Komiya, Y. Ando, H. Eisaki, and S. Uchida, Phys. Rev. Lett. **103**, 037004 (2009).
49. J. Graf, G.-H. Gweon, and A. Lanzara, Physica C (Amsterdam) **460**, 194 (2007).
50. K. Byczuk, M. Kollar, K. Held, Y.-F. Yang, I. A. Nekrasov, Th. Pruschke, and D. Vollhardt, Nat. Phys. **3**, 168 (2007).
51. S. G. Ovchinnikov and S. V. Nikolaev, JETP Lett. **93** (9), 517 (2011).

Translated by N. Wadhwa